ACS APPLIED MATERIALS & INTERFACES

www.acsami.org

Research Article

Roll-to-Roll Production of Electrocatalysts Achieving High-Current Alkaline Water Splitting

Yanita Devi, Po-Jen Huang, Wen-Tai Chen, Ren-Huai Jhang, and Chun-Hu Chen*

Cite This: *ACS Appl. Mater. Interfaces* 2023, 15, 9231−9239

Read Online

ACCESS | Metrics & More | Article Recommendations | Supporting Information

ABSTRACT: Scalable production of electrocatalysts capable of performing high-current water splitting is crucial to support green energy utilization. We adopted acidic redox-assisted deposition (ARD) to realize the continuous roll-to-roll fabrication of a strongly adherent cobalt manganese oxyhydroxide (CMOH) film on Ni foam under ambient conditions in water. The as-fabricated products show uniform CMOH coverage and oxygen evolution activities with dimensions as large as 5 m length by 0.25 m width. Also, we converted CMOH into a metallic form (denoted as CM) with the preserved high adhesion to serve as a high-current hydrogen evolution electrocatalyst. Our results reveal that the insufficient adhesion of powder forms electrocatalysts (i.e., Pt and RuO_2 as benchmarks), even with the binder, at high-current electrolysis (>1000 mA) can be solved using the fabricated CM||CMOH cell. With an active area of 1 cm × 1 cm assembly in anion exchange membrane (AEM) electrolyzers, we observed the remarkable record of alkaline electrolysis stably at 5000 mA. This result established a new benchmark record on the high-current water splitting research.

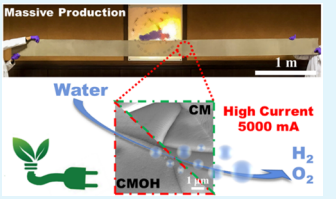

KEYWORDS: *water splitting, acidic redox-assisted deposition, anion exchange membrane, scalable production, oxygen evolution*

1. INTRODUCTION

Massive-scale energy storage is urgently needed for the commercialization of green energy (e.g., wind and solar power) to achieve the goal of carbon neutralization by 2050.[1−3] Reversible hydrogen cycle mediated by water splitting and hydrogen−oxygen recombination by fuel cells have become a promising sustainable approach toward massive energy storage capable of buffering the intermittent supply of green energy.[4−6] To effectively capture peak outputs of green energy, high-current water splitting is, therefore, needed.[7] The application of this technology remains difficult due to intensive gas bubbling at the electrode water−electrocatalyst interfaces (also known as the triple-phase boundary region), generally resulting in electrocatalysts peeling off from the electrodes.[8,9] Benchmark electrocatalysts for water splitting like IrO_2, RuO_2, and Pt are in powder form and require binders (e.g., Nafion) to gain proper adhesion on electrodes.[10,11] In a high-current water splitting situation, however, high amounts of binder would be needed to ensure enough electrocatalyst adhesion and prevent peeling off. As such, significantly decreased electrocatalytic performance is anticipated with too much amount of nonconductive organic binders covering the electrocatalysts.[12,13] The critical criteria for high-current electrolysis should first focus on realizing strong electrocatalyst adhesion on electrodes without using binders.

Scalable production of electrocatalysts is, of course, also an essential part of realizing the commercialization of hydrogen energy.[14] Continuous roll-to-roll fabrication of a thin film is one of the simplest scaled-up methods, however, the capability of conducting liquid phase deposition under ambient conditions is needed.[15] Our prior research has presented the possibility of utilizing acidic redox-assisted deposition (ARD) to accomplish thickness-controllable deposition of multinary metal oxide thin films, which exhibit strong adhesion on generic substrates, for diverse applications, such as anti-bacterial, Li-ion battery, and so on.[8,16,17] The mechanism studies show a critical role of metal-containing oxidants (e.g., MnO_4^-, FeO_4^{2-}, etc.) in corroding top surfaces of the substrate, recognized as "adhestaining" characteristics, to achieve strong adhesion.[18−21] After the adhestaining behavior (also known as surface corrosion) of permanganate to yield the very first base layer, the subsequent growth formation of the Co−Mn network connected by the oxygen bridge continues the film growth.[17,18] Furthermore, ARD was shown to be capable of depositing cobalt manganese oxyhydroxide (CMOH) on a wide variety of substrates, such as rigid glass, poly(ethylene terephthalate) (PET), wood, copper foils, carbon cloth, and glassy carbon electrodes (GCEs). These as-yield depositions can handle harsh peel-off and folding tests.[18,22] The amorphous structure of the resultant films also helps with strong adhesion.[23] The redox feature of ARD does not require the substrates to be conductive, in contrast to in situ growth techniques via electrodeposition. These features

Received: November 2, 2022
Accepted: January 27, 2023
Published: February 8, 2023

https://doi.org/10.1021/acsami.2c19710
ACS Appl. Mater. Interfaces 2023, 15, 9231−9239

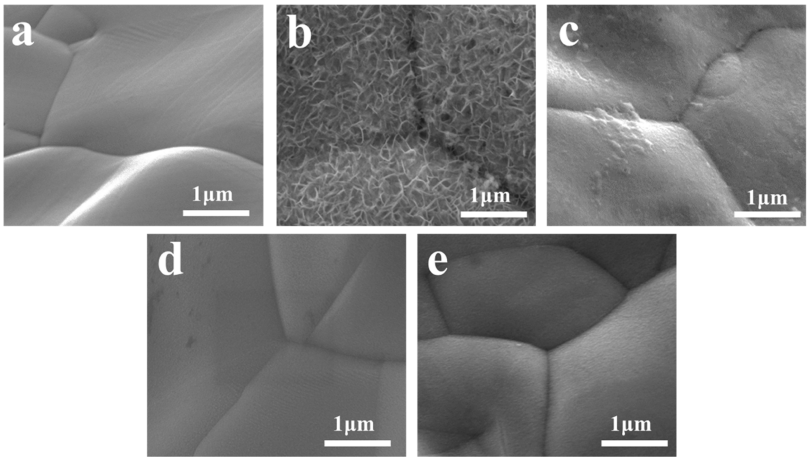

Figure 1. SEM images reveal the surface features of (a) blank Ni foams, (b) CMOH-1x, (c) CMOH-3x, (d) CMOH-5x, and (e) CMOH-7x electrodes.

enable ARD to easily accomplish multimetal incorporation in an individual single-oxide sample and thus highly suitable to be adopted in roll-to-roll fabrication for massive production of sought-after multinary electrocatalysts with strong adhesion.

Recently, most of the water splitting research has reached a range of 500−1500 mA cm^{-2}, categorized as a high-current density benchmark,[22,24−27] particularly for those involving thin-film electrocatalysis.[22,28] These research works concentrate on achieving performance improvements, such as smaller onset and overpotentials at a certain current density of electrocatalysts with small dimensions/sizes.[27,29] Although an ultrahigh current density (2.4−25 A cm^{-2}) was achieved, the practical application of most electrocatalysts with small active areas (e.g., 0.09−0.45 cm^2) toward massive scale electrolysis remains doubtful.[30,31] Some reported catalysts run up to 8 A current with a 20 cm^2 catalyst area but the obtained overall current density of 0.4 A cm^{-2} is still relatively small.[32] Demonstration of continuous and scalable fabrication of active electrocatalysts for both hydrogen and oxygen evolution reactions (HERs and OERs, respectively) has not yet been recognized in the literature. Key discussions regarding principles and guidelines to achieve high-current electrolysis of water are also absent.

In this work, cobalt manganese oxyhydroxide (CMOH) and cobalt manganese alloy (CM) thin-film electrocatalysts active for OER and HER, respectively, are fabricated by a scalable roll-to-roll process via ARD at room temperature. An alkaline anion exchange membrane (AEM) electrolyzer assembly of CM||CMOH can handle 5000 mA cm^{-2} current density operating with an actual current of 5000 mA and operate stably for 30 h. The scaled-up uniform fabrication of these electrocatalysts on nickel foam (Ni foam) electrodes with massive dimensions of up to 5 by 0.25 m was successfully realized and demonstrated. We utilized the strong adhesion properties of CMOH for the OER side and its metallic form, CM, for the HER side, to obtain durable electrocatalysts that can withstand high-current water splitting. Intrinsically strong adhesion of electrocatalysts formed using ARD eliminates the need for organic binders that suppress the surface-active sites. Our results and comparison studies highlight that the insufficient adhesion of benchmark electrocatalysts (e.g., Pt, RuO_2) needs to be addressed before high-current water splitting can be achieved.

2. RESULTS AND DISCUSSION

Amorphous cobalt (Co^{III}) manganese (Mn^{IV}) oxyhydroxide films can be prepared by a simple ARD process through an aqueous reaction of cobalt(II) acetate and potassium permanganate(VII) under ambient conditions without external heating.[18] Single dipping of the substrates (i.e., Ni foam) into the aqueous mixture for 15 min is sufficient to complete the deposition. A deposition time of 15 min was chosen for optimal product deposition since, according to previous research,[18] extending deposition time to 60 min showed no significant changes in the OER activity. These synthesis conditions are referenced and extended to the roll-to-roll fabrication later in this article. The main reaction is shown below[18]

$$9Co^{2+}_{(aq)} + 3Mn^{VII}O^{-}_{4(aq)} + 14H_2O_{(l)} \rightarrow Co^{III}_9Mn^{IV}_3O_{26}H_{13(s)} + 15H^{+}_{(aq)} \quad (1)$$

This redox reaction leads to a highly homogeneous distribution of metal cations in the oxide products.[33] To realize a highly reliable roll-to-roll process, we kept the process temperatures at room temperature but varied the precursor concentrations to optimize the electrocatalyst performance since our earlier studies have shown the product irreproducibility highly sensitive to the temperatures of the ARD reaction bath, particularly above 40−50 °C. We defined the reaction mixture of 20 mM Co^{2+} and 6.7 mM MnO_4^- precursors as the reference basis (the product denoted as CMOH-1x) and increased the concentrations of both precursors to three times (3x), five times (5x), and seven times (7x), with the corresponding products denoted as CMOH-3x, CMOH-5x, and CMOH-7x, respectively (see the Method Section in the Supporting Information).

2.1. Concentration-Dependent Deposition of Electrocatalysts. ARD is known to produce thin films of CMOH with amorphous characteristics for OER electrocatalysis.[18] The scanning electron microscopy (SEM) images of the resulting film show different characteristics as the concentration of the precursors changes (Figure 1). Figure 1b shows that CMOH-1x has continuous flake-like features on the Ni foam surface.[33] In CMOH-3x (Figure 1c), the flake-like features disappear, and only the bumpy surface of the deposition can be observed. In CMOH-5x and CMOH-7x (Figure 1d,e), no appreciable

https://doi.org/10.1021/acsami.2c19710
ACS Appl. Mater. Interfaces 2023, 15, 9231−9239

feature is visible despite the difference in concentrations of precursors. All of the products show a similar Co/Mn ratio of 2:1 based on the inductively coupled plasma mass spectroscopy (ICP-MS) results (Table 1), indicating the successful

Table 1. ICP Result in Different Precursor Concentrations of the CMOH Film

sample	Co[a]	Mn[a]	Co/Mn (molar ratio)
CMOH-1x	3.68 ppm	1.88 ppm	2:1
CMOH-3x	2.45 ppm	1.24 ppm	2:1
CMOH-5x	2.49 ppm	1.12 ppm	2:1
CMOH-7x	1.36 ppm	0.79 ppm	2:1

[a]Concentration was measured in 10 mL of acid solvent.

deposition in both CMOH-5x and CMOH-7x, even with no visible features in the SEM images. Yet, the increased concentrations of precursors gradually decrease the total amounts of deposited cobalt and manganese (see Table 1). Together with the SEM results, a higher concentration of cobalt(II) acetate leads to thinner coatings. The presence of acetate anion from the precursor inhibits the film growth due to its capability of coordinating to cobalt, consistent with the previous studies.[18] This inhibition would be even more prominent with the presence of ethylenediaminetetraacetic acid (EDTA) anions. This inhibition effect of acetate anion allows a controllable growth of film thickness. Furthermore, acetate anions can act as a buffer to limit possible pH changes if the great amount of precursors was used to conduct ARD. In CMOH-7x, the concentration of the acetate anion is too high, and thus, the film is barely deposited. The deposited thin films were subjected to X-ray photoelectron spectroscopy (XPS) to reveal the oxidation states of Co and Mn in the film products (Figures S2 and S3). The presence of Co(III) was observed in all samples based on the XPS peaks at 795.4, 780.1, and 789.8 eV corresponding to Co $2p_{1/2}$, Co $2p_{3/2}$, and Co $2p_{3/2}$ satellite peaks, respectively. The manganese present in all of the thin-film samples exists as Mn(IV) species based on the XPS results of Mn $2p_{3/2}$ and $2p_{1/2}$ at 642 and 653.5 eV, respectively. These XPS results confirm the conversion of Co(II)/Mn(VII) in the precursor solutions to Co(III)/Mn(IV) during the formation of CMOH coating, following eq 1.[8,18,34] Energy-dispersive X-ray (EDX) mapping was used to analyze the cobalt and manganese distribution on Ni foam. The results show a uniform distribution of cobalt and manganese over the entire coated area (Figure S4).

We conducted all of the electrochemical tests in this work on Ni foam using iron-purified KOH.[35,36] The linear sweep voltammetry (LSV) measurement of the deposited samples was carried out in a three-electrode system first to evaluate the alkaline OER performance (Figure 2a). The bare Ni foam substrates show no significant OER activity up to 1.55 V, while the CMOH samples exhibit obvious OER activities. The overpotentials at 10 mA cm^{-2} are 310 mV for CMOH-1x, 310 mV for CMOH-3x, 300 mV for CMOH-5x, and 320 mV for CMOH-7x, as shown in Figure 2a. The sequence shows that CMOH-5x gives the strongest OER activities (the smallest overpotential), followed by CMOH-3x, CMOH-1x, and CMOH-7x. From the result on the Tafel slope of these films (Figure S5), CMOH-5x shows the lowest slope (42 mV/decay) compared to the others (CMOH-3x < CMOH-1x < CMOH-7x), showing that electrocatalytic kinetics of OER in CMOH-5x is superior to all of the others. The electrochemical

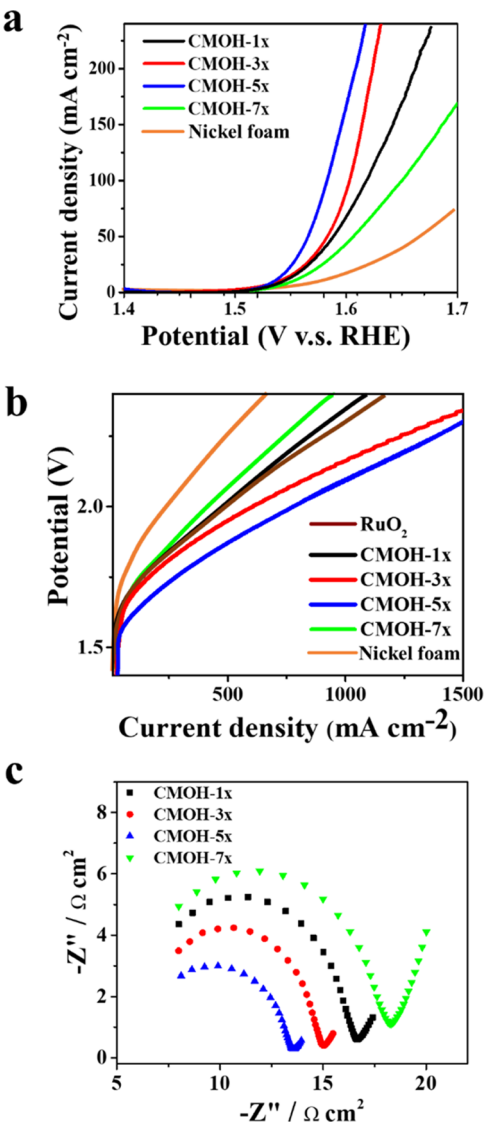

Figure 2. Electrocatalytic performance of the CMOH samples prepared in different precursor solution concentrations. Comparison of the linear sweep voltammetry curves in (a) the three-electrode system and (b) the AEM device with 1 × 1 cm^2 electrode active area (in 1 M iron-purified KOH electrolytes). (c) Impedance curve of the film-coated gold substrate (in 0.1 M iron-purified KOH).

active surface area (ECSA) also shows an increasing trend of CMOH-7x < CMOH-1x < CMOH-3x ≪ CMOH-5x (Figure S6 and Table S2). One sees that CMOH-5x has the highest ECSA value while that of CMOH-7x is the smallest. Since the amounts of active sites usually are proportional to the loading mass, this data suggests that CMOH-5x has the highest quantity of active sites but not possessing the highest loading mass (see Figure 1). Thus, the higher precursor concentrations do not necessarily yield increased amounts of active sites.

The impedance curves (Figure 2c) indicate that CMOH-5x possesses the smallest charge transfer resistance (CMOH-5x < CMOH-3x < CMOH-1x < CMOH-7x), even though all of the samples show similar elemental compositions. Compared to CMOH-1x and CMOH-3x, the relatively thinner thickness of CMOH-5x most likely contributes to such impedance results. Accordingly, CMOH-7x with the lowest film loadings should exhibit the smallest charge transfer resistance, but that goes to CMOH-5x, revealing that a certain level of electrocatalyst

https://doi.org/10.1021/acsami.2c19710
ACS Appl. Mater. Interfaces 2023, 15, 9231−9239

deposition enhances the charge transfer at the heterojunction sites between the film and the substrate. The higher ECSA and more rapid charge transfer in CMOH-5x make the catalyst outperform the others. Taking into consideration all of these results, CMOH-5x is selected to be the optimal condition for roll-to-roll large-scale fabrication and high-current water splitting applications discussed later in this work.

Mechanisms for the enhancement of electrocatalyst performance can be recognized from various points of view, such as high catalyst loading, high catalyst density, or hydrophilicity.[37,38] Based on our previous in situ Raman study of CMOH, the layered hexagonal CoO_2 was found and that corresponds to Co^{3+}/Co^{4+} activation in OER.[8] Amorphous characteristics of CMOH lower the OER activation barrier, compared to the crystalline counterparts. Another reason that also enhances the activity is the Mn^{4+} substitution by Co^{3+} or Mn^{3+} which, as a result, creates cation vacancies due to the need for charge compensation in the structure. These defects and the homogeneous distribution of constituent metals in the structure could increase material conductivity and thus improve catalytic activities. A further advantage of the CMOH thin-film catalyst is the thickness that can be controlled to reach an optimal level that leads to a low interfacial barrier, facilitating better charge transport during electrocatalysis.[18]

The composition of Co/Mn of the product (based on the ICP data), regardless of the concentration of the precursors, is lower than that (Co/Mn = 3/1) prepared by a batch reactor at 80 °C in the earlier work.[18] The lowered Co/Mn ratios should be due to the room temperature conditions. The optimal Co/Mn ratios have been systematically studied in the precursor ranges (Co/Mn) of 9:1 to 1:3, and the optimal composition should lie between Co/Mn of 4:1 to 5:1. Yet, our studies also reveal that the elemental compositions are not the only concern in achieving the highest OER activities. Other properties dependent on the compositions such as electrical resistivity, adhesion, surface area, and thickness are also critical. According to the ICP results of CMOH films, the equation that corresponds to the product composition is shown below

$$9Co^{2+}_{(aq)} + 3Mn^{VII}O^{-}_{4(aq)} + 8H_2O_{(l)} \rightarrow Co^{III}_{6}Mn^{IV}_{3}O_{20}H_{10(s)} + 3Co^{3+}_{(aq)} + 6H^{+}_{(aq)} \quad (2)$$

Since the precursor ratio that we used is 3:1, there is a certain amount of free Co^{3+} in the solution that is not incorporated into the CMOH film during the formation. The free Co^{3+} may be chelated by the acetate ligands in the solution.[18]

2.2. Large-Scale Roll-to-Roll Fabrication. Roll-to-roll processing was adopted for mass production of the electrocatalysts in a large quantity and continuous manner. As illustrated in Figure 3a, Ni foams are used as continuous substrates to pass through the reaction mixture (i.e., the CMOH-5x recipe) under ambient conditions. A video clip demonstrating the whole rolling process is provided (see Movie S1). The roll-to-roll setup was built with dimension details as shown in Figure S14. In our demonstration, 5 m (length) by 0.25 m (width) pristine Ni foams experienced a 15 min contact with the precursor solution at room temperature (28−30 °C). The detailed process is explained further in the Method section.

Since the precursor concentrations of the reaction bath would gradually become lower, the reaction rates also become slower. However, the presence of acetate ions can also

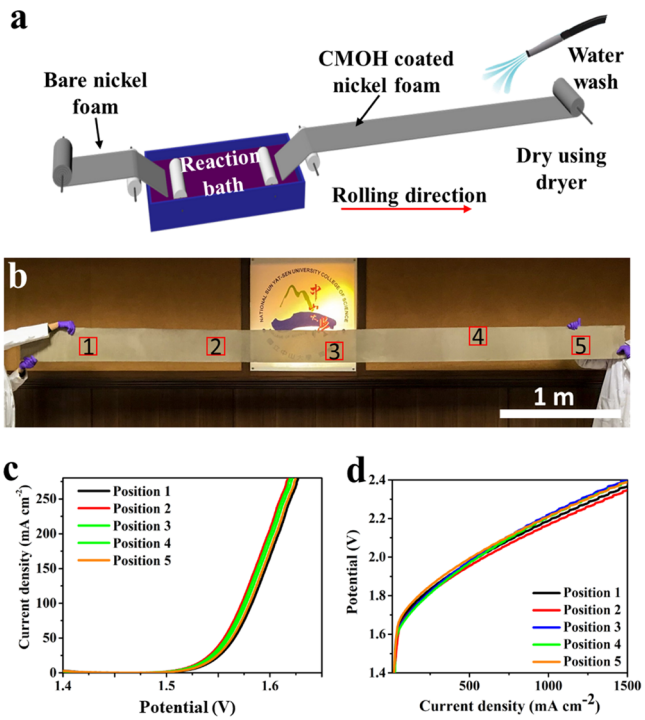

Figure 3. Large-scale production of the CMOH film. (a) Scheme of the roll-to-roll process for large-scale CMOH production. (b) Photograph of CMOH-5x deposited on a Ni foam (5 × 0.25 m^2) using the large-scale roll-to-roll method; the 1 to 5 positions labeled on the photograph indicate the different sampling locations for material characterization and OER tests. The OER catalytic performance of the 1 to 5 positions is shown in panel (c). (d) Water splitting results using samples of the 1 to 5 positions in an AEM device with 1 × 1 cm^2 electrode active area. These electrochemical and water splitting tests are all measured using 1 M iron-purified KOH.

effectively slow down the reaction rates, as indicated by the reduced deposition rates. Such behavior gives a wide window of deposition time, during which the changes in precursor concentrations are small. Thus, a long deposition time is needed for obvious concentration decay of the precursors. This can be supported by the nearly identical OER activity by sampling the entire 5 m long CMOH after the 2 h deposition. Detailed study of the precursor consumption rates of the roll-to-roll process requires a prolonged time.

Figure 3b shows the photographs of the products after the roll-to-roll process. Five different spots (locations 1 to 5) were selected for inspection and characterization to ensure the uniformity of the product. The SEM images of these spots (Figure S7) show a highly similar appearance to each other and also to that of CMOH-5x obtained by the batch synthesis (shown in Figure 1d). In addition, the results of their OER performance are nearly identical from spot to spot (Figure 3c,d) and are also close to the batch-synthesized products (Figure 2a,b). The uniformity in the SEM images and OER performance among the inspected five spots shows that, despite the simplicity of the setup of the manual rolling process, the acetate−ligand coordination and the resulting self-limiting growth in ARD still enable a highly reliable film quality control. A small variation in the electrochemical activity between the samples made by the batch-type and roll-to-roll fabrication is likely due to the different cleaning processes of the Ni foam substrate.

https://doi.org/10.1021/acsami.2c19710
ACS Appl. Mater. Interfaces 2023, 15, 9231−9239

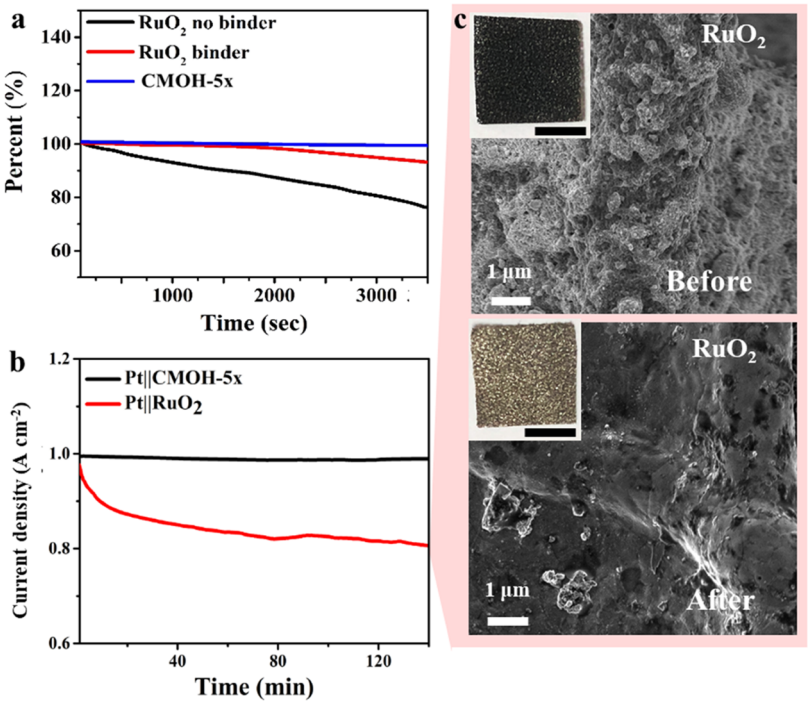

Figure 4. Stability of the OER catalyst and the peeling off problem. (a) Stability of current response (by referencing the starting current at 400 mA) of benchmark RuO_2 with and without the presence of binder and CMOH-5x without binder. (b) Stability results of Pt||CMOH-5x vs Pt||RuO_2 at 1000 mA for 180 min. (c) Corresponding SEM images before and after the stability tests; insets show the appearance of the RuO_2-deposited nickel foam electrode (scale bar = 5 mm).

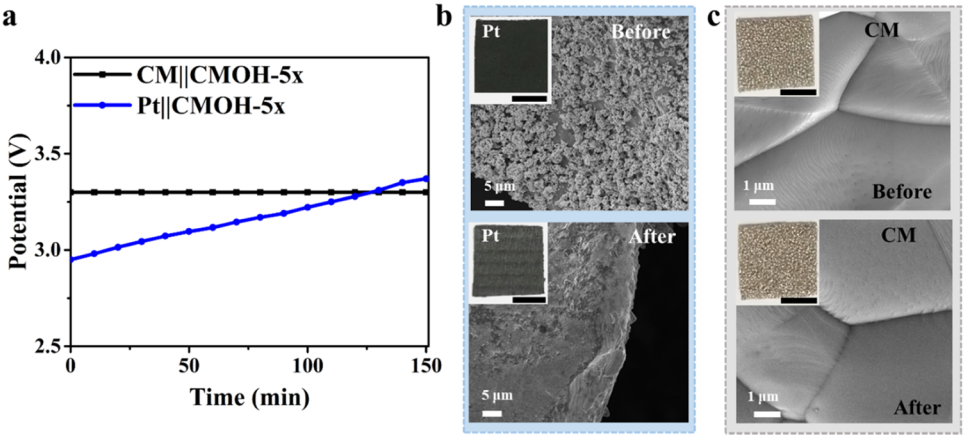

Figure 5. Comparison of the AEM operation stability at a high current of water splitting. (a) Comparison of stability performance of CM||CMOH-5x and Pt||CMOH-5x at 3000 mA cm^{-2} for 150 min. The SEM images of (b) Pt and (c) CM before and after the i–t stability test at 3000 mA for 150 min; insets show the photographs of the corresponding electrode (scale bar = 5 mm).

2.3. Electrocatalyst Adhesion under Large Current Electrolysis. To highlight the crucial roles of electrocatalyst's adhesion properties for high-current electrolysis, we conducted the comparison of CMOH-5x to the benchmark binder-applied and binder-free RuO_2 (Figure 4a). The current density of the binder-free RuO_2 was significantly decreased by 20% after 3500 s by starting at 400 mA cm^{-2}, while that of the binder-applied RuO_2 shows a small decrease of 3%. As expected, powder form RuO_2 relies on binders to acquire proper adhesion to exhibit electrochemical activity but the use of too much amount of binders is shown to weaken the intrinsic electrocatalytic activity (Figure S8). On the other hand, thin-film-form CMOH-5x shows a highly stable current under the same conditions without the need for any binders, emphasizing the importance of strong adhesion toward high-current water splitting.

We further conducted the adhesion tests in AEM cells. The two cells were assembled with CMOH-5x and binder-applied RuO_2 at the OER side and commercial Pt at the HER side for both cells; these cells are denoted as Pt||CMOH-5x and Pt||RuO_2, respectively. With the cell operation starting at 1000 mA cm^{-2}, the currents of Pt||RuO_2 cells gradually decrease by more than 30% in 180 min, while CMOH-5x continues to perform stable water splitting without appreciable current decay (Figure 4b). The RuO_2-loaded electrode of Pt||RuO_2 shows a significant color fading (see the appearance comparison before and after 180 min operation of water splitting, as the inset in Figure 4c). The SEM image comparison (Figure 4c) also

https://doi.org/10.1021/acsami.2c19710
ACS Appl. Mater. Interfaces 2023, 15, 9231−9239

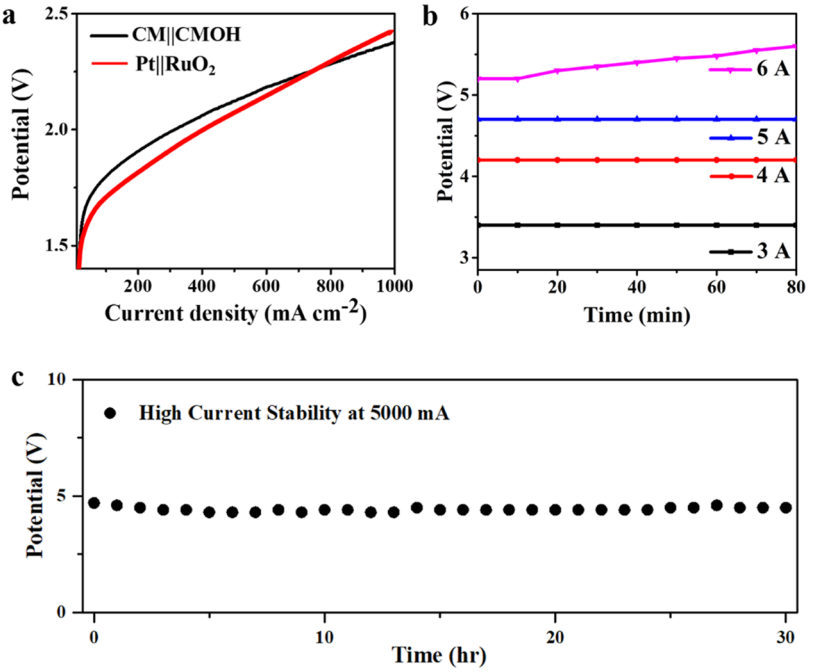

Figure 6. Performance and stability of CM||CMOH-5x on the AEM device. (a) Linear sweep voltammetry comparison of Pt||RuO_2 and CM||CMOH-5x in the AEM cell. (b) Stability of CM||CMOH-5x on the AEM device under different high-current conditions. (c) Long-term stability test of CM||CMOH-5x under 5000 mA cm^{-2} for 30 h. These electrochemical and water splitting tests are all measured using 1 M iron-purified KOH.

exhibits a significant loss of RuO_2 powder after the 1000 mA operation exposing the bare Ni foam surface. These results verify that the superior adhesion of CMOH-5x on the OER side is critical to realizing high-current water splitting.

The same adhesion issue shall also impact the hydrogen evolution reaction (HER) under high-current water splitting. Pt loss may be observed in the tests of Pt||RuO_2 and Pt||CMOH-5x at higher currents. To overcome this issue, our strategy was to utilize the strong adhesion of CMOH by turning CMOH into its reduced form, since, in principle, HER generally requires reductive electrocatalysts. After having CMOH-5x reduced in a H_2 atmosphere at 1000 °C (see the Supporting Information for the detailed procedure and characterization), the product denoted as CM is likely to have an alloy phase (also see Figure S9 for the appearance after the reduction). The XRD patterns (Figure S10a) show a high similarity of crystal parameters between metallic cobalt and manganese phases corresponding to Co^0 (JCPDS 89-4307) and Mn^0 (JCPDS 88-2327). Such features generally suggest an easy formation of a homogeneous solution solid between Co and Mn. The residual signals corresponding to manganese monoxide (JCPDS 02-1158) were noticed. The spectra of X-ray absorption near-edge structure (XANES) for Co and Mn K-edge in Figure S10b,c also show a metallic form of cobalt with peaks at 7707, 7712, and 7725 eV[39] and manganese with peaks at 6541, 6546, and 6555 eV.[40] The LSV of CM (Figure S10d) shows the improved electrocatalytic activity toward HER, as compared to the bare Ni foam substrate.

2.4. AEM Cell Performance at High-Current Water Splitting. To test the adhesion of the as-generated bimetallic alloy CM, two AEM cells of CM||CMOH-5x and Pt||CMOH-5x were fabricated (see the Supporting Information) and operated at an ultrahigh current of 3000 mA cm^{-2} for a clearer comparison. Figure 5a shows a stable operation of the CM||CMOH-5x cell in the 150 min performance stability test while the Pt||CMOH-5x cell shows an electrocatalytic decay characterized by the observed potential increase of 0.5 V. Inspecting the appearance of the Pt electrode of the cell after the operation clearly shows many faded areas/spots over the entire sample, as compared to the sample's color before the test (inset of Figure 5b). The SEM images further support the Pt peel-off from the Ni foam during the test (Figure 5b). On the other hand, both the CM and CMOH-5x electrodes in the CM||CMOH-5x cell show no appreciable changes after the 3000 mA tests as indicated in both the SEM image and photograph appearance (Figures 5c and S11). These results indicate that the strong adhesion of both CM and CMOH is highly essential for high-current water splitting at 3000 mA or above. The high Faraday efficiency (>98.5%) of the CM||CMOH-5x cell also suggests negligible side reaction or catalyst decomposition (Figure S12).

We also compared the full cell performance between CM||CMOH-5x and benchmark Pt||RuO_2 as shown in Figure 6a. The noble metal group-free CM||CMOH-5x cells exhibit a nearly comparable (yet, still slightly weaker) electrolysis activity to Pt||RuO_2. The observed trend is that CM||CMOH-5x shows superior performance beyond a high-current region (>800 mA cm^{-2}). At a large current density (1000 mA cm^{-2}), our CMOH-5x exhibits a potential of 2.2 V. To test the maximum current density of water splitting that the CM||CMOH-5x cell is capable of, we systematically increased the current density from 3000 to 6000 mA cm^{-2} with an interval of 1000 mA cm^{-2}. Figure 6b shows the steady operation of the cell up to 5000 mA cm^{-2} for 80 min, while a gradual increase of the operation potential is observed at 6000 mA cm^{-2}. The results suggest a maximum, durable operation current for CM||CMOH in between 5000−6000 mA cm^{-2}, an electron density that even the benchmark electrocatalysts like RuO_2 and Pt cannot handle. The strong adhesion electrocatalysts achieve the durable water splitting capability for a total current as high

https://doi.org/10.1021/acsami.2c19710
ACS Appl. Mater. Interfaces 2023, 15, 9231−9239

as 5000 mA, superior to most of the current literature using first-transition metal oxides in powder forms.[19,41] A longer stability test at 5000 mA cm^{-2} showed that the CM||CMOH-5x cell can run up to 30 h without significant change in its performance (Figure 6c). In addition, the LSV result for the cell that was subjected to 6000 mA cm^{-2} shows highly similar results to that before the high-current tests (Figure S13). The ICP analysis of the iron-purified KOH electrolyte after the high-current tests (from 5000 to 6000 mA) shows no sign of Co or Mn dissolution into the electrolyte (Table S1). These data together suggest that CM and CMOH-5x almost remain intact after such high-current tests. Before a detailed investigation, the maximum current of 5000 mA is most likely limited by other parts/operation conditions of the AEM cells (such as membrane, flow rates, conductivities, etc.),[42] rather than any forms of the degradation of CM or CMOH-5x. The possibility of achieving an even higher current toward electrolysis is promising through the further improvement of the weak components of AEM cells. Furthermore, CM||CMOH possesses strong adhesion on both the anode and cathode, giving the advantage to avoid electrocatalyst peel-off against high-current electrolysis.

3. CONCLUSIONS

In summary, strong adhesion CMOH and CM thin-film electrocatalysts have been demonstrated to be crucial for achieving high-current electrolysis >5000 mA cm^{-2}. The nature of ARD enables the success of adopting roll-to-roll fabrication for scalable production of CMOH and CM on the Ni foam substrate. The combination of high-current electrolysis and mass production of electrodes represents a promising future for green hydrogen commercialization. Through modified versions of the ARD approach, undoubtedly, one can easily produce complex multimetal oxide films that are more advanced than CMOH. In addition to the electrochemistry field, this ARD approach may also bring revolutionary impacts on all of the related subjects involving metal oxide semiconductors.

4. METHODS

4.1. Large-Scale CMOH Fabrication Using Roll-to-Roll Process. Large-size nickel foam (Ni foam) with 5 m length by 0.25 m width dimensions was precleaned (using the procedure mentioned in the Supporting Information) but without the O_2 plasma treatment step. The precursor mixture used in the CMOH-5x synthesis (all of the CMOH batch synthesis is mentioned in the Supporting Information) was adopted for this roll-to-roll fabrication, in which 210 mmol of cobalt acetate and 70 mmol of potassium permanganate were dissolved in 2100 mL of deionized (DI) water. The Ni foam was placed onto the setup of roller bars with a certain part of the loaded Ni foam directly in contact with the precursor mixture in the pool (see the demonstration in Movie S1). We built a rolling device using 1/2″ diameter poly(vinyl chloride) (PVC) pipes to fit a 25 cm width by 5 m long rolled Ni foam as the substrate (shown in Figure S14). The loaded Ni foam belt translated with a speed of 4 ± 1 cm/min. The products were collected on the opposing side (see Movie S1). Every spot of the loaded Ni foam experienced a 15 min contact with a reaction bath at room temperature (about 28−30 °C). After the roll-to-roll process, the powder samples generated in the reaction mixture of the pool were also collected as alternative reference samples used in the reduction process to CM (the CM synthesis procedure is mentioned in the Supporting Information) in Section 2.3.

ASSOCIATED CONTENT

Supporting Information

The Supporting Information is available free of charge at https://pubs.acs.org/doi/10.1021/acsami.2c19710.

Small-scale CMOH deposition on Ni foam by batch processing, synthesis of CM from CMOH, material characterization, and electrochemical test; EDX elemental distribution of CMOH-5x; SEM result of the large-scale roll-to-roll production; XRD graph of the CMOH powder; XPS results on the different concentrations of the CMOH film and CMOH-5x film; C_{dl} and ECSA data of the different concentrations of CMOH deposited on a gold substrate; performance comparison on the RDE electrode of the RuO_2 catalyst with and without binder; the digital image of CMOH-5x film deposited on the Ni foam before and after reduction to CM at 1000 °C appearance; XRD characterization result and XANES spectra of the CM powder; HER performance of CM deposited on Ni foam; faraday efficiency result of CM||CMOH-5x cell on AEM device at 500 mA, for 1 h (1 M KOH), and performance of CM||CMOH-5x cell before and after 6000 mA test (PDF)

Video clip demonstrating the whole rolling process is provided (Movie S1) (MP4)

AUTHOR INFORMATION

Corresponding Author

Chun-Hu Chen − *Department of Chemistry, National Sun Yat-Sen University, Kaohsiung 80424, Taiwan;* orcid.org/0000-0002-3512-6880; Phone: 886-7-525-2000; Email: chunhu.chen@mail.nsysu.edu.tw; Fax: 886-7-525-3908

Authors

Yanita Devi − *Department of Chemistry, National Sun Yat-Sen University, Kaohsiung 80424, Taiwan;* orcid.org/0000-0002-3526-2145

Po-Jen Huang − *Department of Chemistry, National Sun Yat-Sen University, Kaohsiung 80424, Taiwan*

Wen-Tai Chen − *Department of Chemistry, National Sun Yat-Sen University, Kaohsiung 80424, Taiwan*

Ren-Huai Jhang − *Department of Chemistry, National Sun Yat-Sen University, Kaohsiung 80424, Taiwan;* orcid.org/0000-0002-8439-5446

Complete contact information is available at: https://pubs.acs.org/10.1021/acsami.2c19710

Author Contributions

The manuscript was written through the contributions of all authors. All authors have given approval for the final version of the manuscript.

Notes

The authors declare no competing financial interest.

ACKNOWLEDGMENTS

The authors acknowledge the financial support from the Ministry of Science and Technology, Taiwan under the grant (MOST-109-2628-M-110-001-MY3). We thank the technical services provided by the National Synchrotron Radiation Research Center in Taiwan.

REFERENCES

(1) Schreyer, F.; Luderer, G.; Rodrigues, R.; Pietzcker, R. C.; Baumstark, L.; Sugiyama, M.; Brecha, R. J.; Ueckerdt, F. Common but Differentiated Leadership: Strategies and Challenges for Carbon Neutrality by 2050 across Industrialized Economies. *Environ. Res. Lett.* **2020**, *15*, No. 114016.

(2) Schmidt, J.; Gruber, K.; Klingler, M.; Klöckl, C.; Ramirez Camargo, L.; Regner, P.; Turkovska, O.; Wehrle, S.; Wetterlund, E. A New Perspective on Global Renewable Energy Systems: Why Trade in Energy Carriers Matters. *Energy Environ. Sci.* **2019**, *12*, 2022−2029.

(3) Zhao, W.; Rubio, S. J. B.; Dang, Y.; Suib, S. L. Green Electrochemical Energy Storage Devices Based on Sustainable Manganese Dioxides. *ACS ES&T Engg* **2022**, *2*, 20−42.

(4) Li, X.; Zhao, L.; Yu, J.; Liu, X.; Zhang, X.; Liu, H.; Zhou, W. Water Splitting: From Electrode to Green Energy System. *Nano-Micro Lett.* **2020**, *12*, No. 131.

(5) Suen, N.-T.; Hung, S.-F.; Quan, Q.; Zhang, N.; Xu, Y.-J.; Chen, H. M. Electrocatalysis for the Oxygen Evolution Reaction: Recent Development and Future Perspectives. *Chem. Soc. Rev.* **2017**, *46*, 337−365.

(6) Faber, M. S.; Jin, S. Earth-Abundant Inorganic Electrocatalysts and Their Nanostructures for Energy Conversion Applications. *Energy Environ. Sci.* **2014**, *7*, 3519−3542.

(7) Seh, Z. W.; Kibsgaard, J.; Dickens, C. F.; Chorkendorff, I.; Nørskov, J. K.; Jaramillo, T. F. Combining Theory and Experiment in Electrocatalysis: Insights into Materials Design. *Science* **2017**, *355*, No. eaad4998.

(8) Shih, M.-C.; Jhang, R.-H.; Tsai, Y.-T.; Huang, C.-W.; Hung, Y., Jr; Liao, M.-Y.; Huang, J.; Chen, C.-H. Discontinuity-Enhanced Thin Film Electrocatalytic Oxygen Evolution. *Small* **2019**, *15*, No. 1903363.

(9) Kou, T.; Wang, S.; Li, Y. Perspective on High-Rate Alkaline Water Splitting. *ACS Mater. Lett.* **2021**, *3*, 224−234.

(10) Liu, D.; Li, X.; Chen, S.; Yan, H.; Wang, C.; Wu, C.; Haleem, Y. A.; Duan, S.; Lu, J.; Ge, B.; et al. Atomically Dispersed Platinum Supported on Curved Carbon Supports for Efficient Electrocatalytic Hydrogen Evolution. *Nat. Energy* **2019**, *4*, 512−518.

(11) Tabassum, L.; Tasnim, H.; Shubhashish, S.; Perera, I.; Bhosale, T.; Li, M.; March, S.; Islam, M. K.; Suib, S. L. Selenium-Doped Copper Oxide Nanoarrays: Robust Electrocatalyst for the Oxygen Evolution Reaction with Ultralow Overpotential. *Appl. Mater. Today* **2022**, *27*, No. 101485.

(12) Wang, H.-Y.; Hsu, Y.-Y.; Chen, R.; Chan, T.-S.; Chen, H. M.; Liu, B. Ni^{3+}-Induced Formation of Active NiOOH on the Spinel Ni−Co Oxide Surface for Efficient Oxygen Evolution Reaction. *Adv. Energy Mater.* **2015**, *5*, No. 1500091.

(13) Yu, Q.; Zhang, Z.; Qiu, S.; Luo, Y.; Liu, Z.; Yang, F.; Liu, H.; Ge, S.; Zou, X.; Ding, B.; et al. A Ta-TaS_2 Monolith Catalyst with Robust and Metallic Interface for Superior Hydrogen Evolution. *Nat. Commun.* **2021**, *12*, No. 6051.

(14) Lee, M. H.; Lim, N.; Ruebusch, D. J.; Jamshidi, A.; Kapadia, R.; Lee, R.; Seok, T. J.; Takei, K.; Cho, K. Y.; Fan, Z.; et al. Roll-to-Roll Anodization and Etching of Aluminum Foils for High-Throughput Surface Nanotexturing. *Nano Lett.* **2011**, *11*, 3425−3430.

(15) Oakes, L.; Hanken, T.; Carter, R.; Yates, W.; Pint, C. L. Roll-to-Roll Nanomanufacturing of Hybrid Nanostructures for Energy Storage Device Design. *ACS Appl. Mater. Interfaces* **2015**, *7*, 14201−14210.

(16) Tsai, Y.-T.; Wu, C.-Y.; Duh, J.-G. Synthesis of Ni-Rich NMC Cathode Material by Redox-Assisted Deposition Method for Lithium Ion Batteries. *Electrochim. Acta* **2021**, *381*, No. 138244.

(17) Huang, H.; Barber, O. W.; Yu, Z.; Park, H.; Hu, X.; Chen, X.; Chen, C.-H.; Hartmann, E. M.; Huang, J. Rub-Resistant Antibacterial Surface Conversion Layer on Stainless Steel. *Adv. Mater. Interfaces* **2022**, *9*, No. 2200251.

(18) Jhang, R.-H.; Yang, C.-Y.; Shih, M.-C.; Ho, J.-Q.; Tsai, Y.-T.; Chen, C.-H. Redox-Assisted Multicomponent Deposition of Ultrathin Amorphous Metal Oxides on Arbitrary Substrates: Highly Durable Cobalt Manganese Oxyhydroxide for Efficient Oxygen Evolution. *J. Mater. Chem. A* **2018**, *6*, 17915−17928.

(19) Liao, P.-C.; Jhang, R.-H.; Chiu, Y.-H.; Valinton, J. A. A.; Yeh, C.-H.; Ebajo, V. D.; Wang, C.-H.; Chen, C.-H. Rock Salt Oxide Hollow Spheres Achieving Durable Performance in Bifunctional Oxygen Energy Cells. *ACS Appl. Energy Mater.* **2021**, *4*, 3448−3459.

(20) Meng, Y.; Song, W.; Huang, H.; Ren, Z.; Chen, S.-Y.; Suib, S. L. Structure−Property Relationship of Bifunctional Mno_2 Nanostructures: Highly Efficient, Ultra-Stable Electrochemical Water Oxidation and Oxygen Reduction Reaction Catalysts Identified in Alkaline Media. *J. Am. Chem. Soc.* **2014**, *136*, 11452−11464.

(21) Ren, Z.; Li, J.; Ren, Y.; Wang, S.; Qiu, Y.; Yu, J. Large-Scale Synthesis of Hybrid Metal Oxides through Metal Redox Mechanism for High-Performance Pseudocapacitors. *Sci. Rep.* **2016**, *6*, No. 20021.

(22) Zhou, H.; Yu, F.; Zhu, Q.; Sun, J.; Qin, F.; Yu, L.; Bao, J.; Yu, Y.; Chen, S.; Ren, Z. Water Splitting by Electrolysis at High Current Densities under 1.6 Volts. *Energy Environ. Sci.* **2018**, *11*, 2858−2864.

(23) Kanan, M. W.; Nocera, D. G. In Situ Formation of an Oxygen-Evolving Catalyst in Neutral Water Containing Phosphate and Co^{2+}. *Science* **2008**, *321*, 1072−1075.

(24) Qian, G.; Chen, J.; Luo, L.; Yu, T.; Wang, Y.; Jiang, W.; Xu, Q.; Feng, S.; Yin, S. Industrially Promising Nanowire Heterostructure Catalyst for Enhancing Overall Water Splitting at Large Current Density. *ACS Sustainable Chem. Eng.* **2020**, *8*, 12063−12071.

(25) Yan, P.; Hu, Y.; Shoko, E.; Isimjan, T. T.; Tian, J.; Yang, X. Hierarchical Core-Shell N-Doped Carbon@FeP_4-CoP Arrays as Robust Bifunctional Electrocatalysts for Overall Water Splitting at High Current Density. *Adv. Mater. Interfaces* **2021**, *8*, No. 2100065.

(26) Wang, P.; Luo, Y.; Zhang, G.; Wu, M.; Chen, Z.; Sun, S.; Shi, Z. MnO_x -Decorated Nickel-Iron Phosphides Nanosheets: Interface Modifications for Robust Overall Water Splitting at Ultra-High Current Densities. *Small* **2022**, *18*, No. 2105803.

(27) Sun, C.; Wang, H.; Ji, S.; Wang, X.; Linkov, V.; Tian, X.; Yao, L.; Zhao, J.; Wang, R. Layer-Structured FeCo Bihydroxide as an Ultra-Stable Bifunctional Electrocatalyst for Water Splitting at High Current Densities. *Sustainable Energy Fuels* **2021**, *5*, 2747−2752.

(28) Zhang, J.; Hu, Y.; Liu, D.; Yu, Y.; Zhang, B. Enhancing Oxygen Evolution Reaction at High Current Densities on Amorphous-Like Ni−Fe−S Ultrathin Nanosheets Via Oxygen Incorporation and Electrochemical Tuning. *Adv. Sci.* **2017**, *4*, No. 1600343.

(29) Wen, S.; Chen, G.; Chen, W.; Li, M.; Ouyang, B.; Wang, X.; Chen, D.; Gong, T.; Zhang, X.; Huang, J.; Ostrikov, K. K. Nb-Doped Layered Feni Phosphide Nanosheets for Highly Efficient Overall Water Splitting under High Current Densities. *J. Mater. Chem. A* **2021**, *9*, 9918−9926.

(30) Yang, F.; Kim, M. J.; Brown, M.; Wiley, B. J. Alkaline Water Electrolysis at 25 A cm^{-2} with a Microfibrous Flow-through Electrode. *Adv. Energy Mater.* **2020**, *10*, No. 2001174.

(31) Zhang, W.; Qi, J.; Liu, K.; Cao, R. A Nickel-Based Integrated Electrode from an Autologous Growth Strategy for Highly Efficient Water Oxidation. *Adv. Energy Mater.* **2016**, *6*, No. 1502489.

(32) Wen, Q.; Yang, K.; Huang, D.; Cheng, G.; Ai, X.; Liu, Y.; Fang, J.; Li, H.; Yu, L.; Zhai, T. Schottky Heterojunction Nanosheet Array Achieving High-Current-Density Oxygen Evolution for Industrial Water Splitting Electrolyzers. *Adv. Energy Mater.* **2021**, *11*, No. 2102353.

(33) Lan, W.-J.; Kuo, C.-C.; Chen, C.-H. Hierarchical Nanostructures with Unique Y-Shaped Interconnection Networks in Manganese Substituted Cobalt Oxides: The Enhancement Effect on Electrochemical Sensing Performance. *Chem. Commun.* **2013**, *49*, 3025−3027.

(34) Kuo, C.-C.; Lan, W.-J.; Chen, C.-H. Redox Preparation of Mixed-Valence Cobalt Manganese Oxide Nanostructured Materials: Highly Efficient Noble Metal-Free Electrocatalysts for Sensing Hydrogen Peroxide. *Nanoscale* **2014**, *6*, 334−341.

(35) Trotochaud, L.; Young, S. L.; Ranney, J. K.; Boettcher, S. W. Nickel−Iron Oxyhydroxide Oxygen-Evolution Electrocatalysts: The Role of Intentional and Incidental Iron Incorporation. *J. Am. Chem. Soc.* **2014**, *136*, 6744−6753.

https://doi.org/10.1021/acsami.2c19710
ACS Appl. Mater. Interfaces 2023, 15, 9231−9239

(36) Burke, M. S.; Kast, M. G.; Trotochaud, L.; Smith, A. M.; Boettcher, S. W. Cobalt−Iron (Oxy)Hydroxide Oxygen Evolution Electrocatalysts: The Role of Structure and Composition on Activity, Stability, and Mechanism. *J. Am. Chem. Soc.* **2015**, *137*, 3638−3648.
(37) Li, H.; Chen, S.; Zhang, Y.; Zhang, Q.; Jia, X.; Zhang, Q.; Gu, L.; Sun, X.; Song, L.; Wang, X. Systematic Design of Superaerophobic Nanotube-Array Electrode Comprised of Transition-Metal Sulfides for Overall Water Splitting. *Nat. Commun.* **2018**, *9*, No. 2452.
(38) Yang, G.; Zhu, J.; Yuan, P.; Hu, Y.; Qu, G.; Lu, B.-A.; Xue, X.; Yin, H.; Cheng, W.; Cheng, J.; et al. Regulating Fe-Spin State by Atomically Dispersed Mn-N in Fe-N-C Catalysts with High Oxygen Reduction Activity. *Nat. Commun.* **2021**, *12*, No. 1734.
(39) Mohandas, J. C.; Gnanamani, M. K.; Jacobs, G.; Ma, W.; Ji, Y.; Khalid, S.; Davis, B. H. Fischer−Tropsch Synthesis: Characterization and Reaction Testing of Cobalt Carbide. *ACS Catal.* **2011**, *1*, 1581−1588.
(40) Manikandan, D.; Yadav, A. K.; Jha, S. N.; Bhattacharyya, D.; Boukhvalov, D. W.; Murugan, R. XANES, EXAFS, EPR, and First-Principles Modeling on Electronic Structure and Ferromagnetism in Mn Doped SnO_2 Quantum Dots. *J. Phys. Chem. C* **2019**, *123*, 3067−3075.
(41) Cai, W.; Yang, H.; Zhang, J.; Chen, H.-C.; Tao, H. B.; Gao, J.; Liu, S.; Liu, W.; Li, X.; Liu, B. Amorphous Multimetal Alloy Oxygen Evolving Catalysts. *ACS Mater. Lett.* **2020**, *2*, 624−632.
(42) Xu, Q.; Oener, S. Z.; Lindquist, G.; Jiang, H.; Li, C.; Boettcher, S. W. Integrated Reference Electrodes in Anion-Exchange-Membrane Electrolyzers: Impact of Stainless-Steel Gas-Diffusion Layers and Internal Mechanical Pressure. *ACS Energy Lett.* **2021**, *6*, 305−312.

https://doi.org/10.1021/acsami.2c19710
ACS Appl. Mater. Interfaces 2023, 15, 9231−9239